Engineering Structures 124 (2016) 49–63

Contents lists available at ScienceDirect

Engineering Structures

journal homepage: www.elsevier.com/locate/engstruct

Seismic behaviors of squat reinforced concrete shear walls under freeze-thaw cycles: A pilot experimental study

Wei Yang [a], Shan-Suo Zheng [a], De-Yi Zhang [a,b,*], Long-Fei Sun [a], Chuan-Lei Gan [a]

[a] Department of Civil Engineering, Xi'an University of Architecture and Technology, Xi'an 710055, China
[b] Department of Civil and Environmental Engineering, University of Waterloo, Waterloo, Ontario N2L 3G1, Canada

ARTICLE INFO

Article history:
Received 26 November 2015
Revised 7 June 2016
Accepted 8 June 2016
Available online 20 June 2016

Keywords:
Freeze-thaw cycles
Squat reinforced concrete shear wall
Seismic performance

ABSTRACT

An experimental study was undertaken to investigate the influence of freeze-thaw cycles (FTCs) on the seismic performance of shear wall specimens. Four identical squat reinforced concrete (RC) shear wall specimens were tested; three were subjected to 100, 200 and 300 FTCs, and the other one was left undisturbed and used as a control specimen. The shear wall specimens were loaded in a reverse cyclic manner, and the principal damage states were investigated throughout the testing process. The responses of the wall specimens were initially dominated by flexural cracking but gradually changed to shear cracking; the damage patterns of the wall specimens gradually changed from diagonal tensile failure to compressive failure, as the number of FTCs increased. Based on the test results of this study, the effects of FTCs on the damage characteristics, hysteretic behavior, ductility, secant stiffness degradation, strength degradation and energy dissipation capacity of the samples were analyzed. The test results indicate that FTCs have significant effects on the seismic performances of shear walls. As the number of FTCs increases, the load-carrying capacity decreases significantly, and the contribution of shear deformation increases significantly. Specimens experiencing more FTCs tend to have larger ductility coefficients and plastic rotation magnitudes. Note that the energy dissipation coefficient and cumulative hysteretic dissipation energy are more sensitive to changes in the number of FTCs than the work index.

© 2016 Elsevier Ltd. All rights reserved.

1. Introduction

It is known that frost action in cold climates is one of the major causes of concrete deterioration [1]. The physical damage of concrete caused by freeze-thaw cycles (FTCs) is usually considered to be a durability issue of concrete surface only, and the FTC influence on concrete mechanical behavior is often not considered [2]. However, for existing buildings, frost action is a long-term process that cannot be observed within a short period until the concrete cover begins to spall. As the number of FTCs increases, buildings become more structurally fragile; thus, a procedure to evaluate the performance of existing buildings under FTCs shall be developed.

In cold regions, such as Northeastern China and Xinjiang Province, Reinforced Concrete (RC) structures experience frost action for long periods each year; the temperature during these periods varies significantly between day and night, providing a natural condition for frost action. In middle and northern Europe, as well as North America, Canada, Japan and Russia, RC structures damages caused by FTCs received significant attention for several decades [3]. For instance, in United States, many RC structures are constructed in extreme cold regions like North Dakota, where the freeze and thaw process becomes a key influence on the mechanical behavior of concrete [4]. In Canada, the infrastructure is deteriorating rapidly because of exposure to cold-climate conditions such as freeze–thaw action, deicing salts and sustained low temperatures [5].

Water is typically splashed onto bridge piers and shear walls and columns of underground parking structures, making the concrete surfaces wet; when temperatures drop below 0 °C, the water freezes. Powers [6,7] reported that as the water in moist concrete freezes, it causes pressure to increase in the pores of the concrete. If this pressure exceeds the tensile strength of the concrete, the cavity will dilate and rupture. The cumulative effect of successive FTCs and the disruption of the concrete's paste and aggregate can eventually cause expansion, cracking, scaling, and crumbling of the concrete.

* Corresponding author at: Department of Civil Engineering, Xi'an University of Architecture and Technology, Xi'an 710055, China.
E-mail addresses: bluceyang1987@163.com (W. Yang), zhengshansuo@263.net (S.-S. Zheng), d56zhang@uwaterloo.ca (D.-Y. Zhang), sunlongfei0218@126.com (L.-F. Sun), chuanlei1990@sina.cn (C.-L. Gan).

http://dx.doi.org/10.1016/j.engstruct.2016.06.013
0141-0296/© 2016 Elsevier Ltd. All rights reserved.

To determine the frost resistance of plain concrete, concrete specimens that are shaped as cylinders, prisms and cubes are often tested with a standard freeze-thaw test (e.g., ASTM C666-92 [8], RILEM TC176-IDC2002 [9] and GB/T50082-2009 [10]). For a reinforced concrete (RC) building, the reinforcement bars meshes and stirrups in the RC components could restrict the propagation of the freeze-thaw cracks and improve the compression and tension strengths of the section core concrete as well as the ductilities of the RC components. However, the freeze-thaw testing method used by the current standards [8–10] does not consider this advantageous confinement effect.

Studies of FTCs have primarily focused on material-level behavior, such as concrete strength and stiffness, stress-strain relationships of concrete, and bond strength [2,11–15], and have not considered the confined concrete strength. Duan [16–18] investigated the stress-strain relationship for stirrup-confined concrete after FTCs by testing two series of concrete specimens. Analytical models for the stress-strain relationship of freeze-thaw unconfined and confined concrete were empirically developed; however, the scope of this study was limited to the material level. The deterioration models for concrete elastic modulus and bond strength subjected to FTCs were adopted to compute the moment-curvature relation of RC beams damaged by FTCs, while the cyclic degradation behavior of strength and stiffness of the specimens damaged by FTCs was not yet investigated [19].

RC buildings are subjected to mechanical loads and environmental effects. However, studies of the cyclic material behavior of concrete damaged by FTCs have been limited to date [2,20], and the cyclic material behavior of confined concrete damaged by FTCs has never been described.

In addition, the deterioration of seismic performance due to cyclic load reversals and frost action is not reported for RC structures in the above analyses. Therefore, this study presents a pilot experimental study of the seismic behaviors of RC shear walls that experience FTCs. This study aims to experimentally investigate the influence of FTCs on the seismic behaviors of RC members and describe the related physical mechanisms behind the experimental phenomena. In this experiment, four identical squat reinforced concrete shear walls were tested at FTCs ranging from 0 times to 300 times under cyclic reversal of loads.

2. Experimental program

2.1. Description of test specimens

Considering the limitation of the dimensions of the environmental chamber used in this study, four identical RC shear wall specimens were designed for testing with various numbers of FTCs and the design parameters of wall specimens were shown in Table 1. The walls constructed were 0.7 m long, 0.7 m high, and 0.1 m thick. The aspect ratio and moment-to-shear ratio of the walls were 1.0 and 1.14, respectively. Boundary elements in the form of beams were set for the shear walls. The concrete clear cover was 10 mm, and the reinforcement used was smooth bars except for deformed bars, which were used as the boundary's longitudinal reinforcement, which consisted of four Grade HRB335 vertical bars. The vertical and horizontal web reinforcements were 6-mm-diameter bars with grade HPB235. Axial and lateral loads were transferred to the walls through the beams constructed over the wall webs. Wall foundations were clamped to the laboratory strong floor. Cross-section and reinforcement details of the four wall specimens are shown in Fig. 1. It should be noted that the shear span ratio of the tested shear wall specimens under FTCs is limited to 1.14, and test on wall specimens with a shear span ratio of 3 under FTCs (which might be dominated by flexural failure) is now on progress and will be reported in the future.

The mixing ratio for C50 concrete was 400 kg/m^3 of cement, 980 kg/m^3 of sand, 810 kg/m^3 of fine gravel, 95 kg/m^3 of water and 80 kg/m^3 of fly ash. Ordinary Portland cement P.O 42.5R and medium sand were used, and the maximum size of the fine gravel particles was 15 mm. Three standard cubic specimens of concrete were prepared under the same conditions as the shear walls. The real strengths of the concrete and the reinforcement bars were determined via material property tests. The average cubic compressive strength of the concrete was 55.08 MPa, and the properties of the reinforcement bars are shown in Table 2.

2.2. Freeze-thaw cycle in the environmental chamber

The environmental chamber, which can simulate various environments such as varying temperature and humidity, salt spray, solar irradiance, acid rain and carbon dioxide levels, was used for the durability testing. The chamber was manufactured by Wuhuancq model (ZHT/W2300) with a temperature range of −20 to 80 °C and dimensions of 2.5 m long, 2 m tall and 2 m wide [21], as shown in Fig. 2(a). The primary technical specifications are:

(1) Temperature range: −20 to 80 °C, temperature departure: ±2 °C, temperature fluctuation ⩽ ±0.5 °C, heating rate: 1–0.7 °C/min (−20 to 80 °C, empty), cooling rate: 1–0.7 °C/min (80 to −20 °C, empty).
(2) Humidity range: 30–98% RH without heating samples, humidity departure: ① 2 to −3% (>75%RH) and ② ±5% (⩽75%RH).

Due to the limited dimensions of the environmental chamber, the wall specimens were divided into shear walls, loading beams and foundation blocks and were subsequently casted together in sequence. The shear wall parts were first casted and cured for 28 days under a natural environment, and then placed in 15–20 °C water for four days before being placed into the environmental chamber, as shown in Fig. 2(b). The freeze-thaw testing process is shown in Fig. 2(c). After the setting cycles were finished, the wall was re-casted with the loading beam and foundation block, as shown in Fig. 2(d).

The environmental parameters of the FTCs are shown in Fig. 3; each freeze-thaw cycle lasted 5.5 h. To produce better freeze-thaw effects, 5 spray cycles were applied before each freeze-thaw cycle began; each spraying cycle lasted for 3 min (1 min of spraying, followed by 2 min without spraying). The freeze-thaw process

Table 1
Design parameters of wall specimens.

Specimen number	λ	Concrete strength grade	n	ρ_{be} (%)	ρ_h (%)	ρ_v (%)	P (kN)	Freeze-thaw cycle (times)
SW-1	1.14	C50	0.2	2.26	0.283	0.320	515.76	0
SW-2	1.14	C50	0.2	2.26	0.283	0.320	515.76	100
SW-3	1.14	C50	0.2	2.26	0.283	0.320	515.76	200
SW-4	1.14	C50	0.2	2.26	0.283	0.320	515.76	300

Notes: λ is the shear span ratio; n is the axial compression ratio; ρ_{be} is the ratio of the flexural reinforcement in the boundary elements; and ρ_h and ρ_v are the ratio of the horizontal web reinforcement and the ratio of the vertical web reinforcement, respectively; P is the axial load.

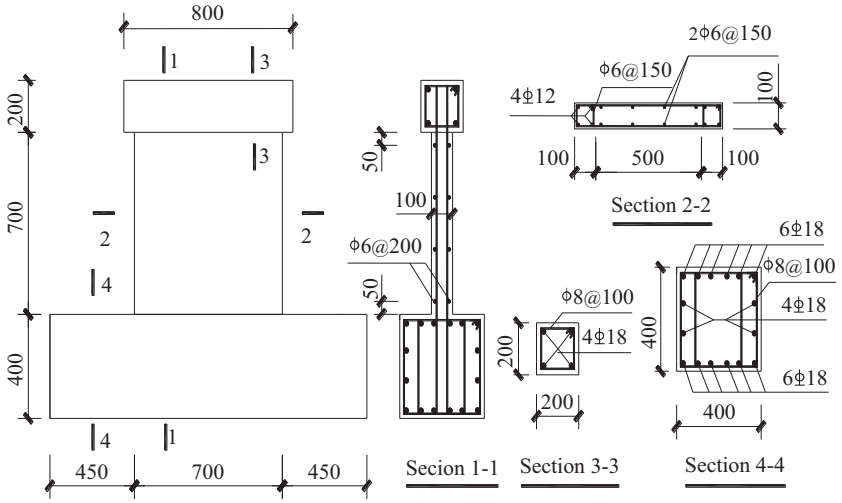

Fig. 1. Dimensions and reinforcement details of the wall specimens (unit: mm).

Table 2
Mechanical properties of the reinforcement bars.

Diameter (mm)	Yielding strength f_y (MPa)	Ultimate strength f_u (MPa)	Elastic modulus E_s (MPa)
∅6	270	470	2.1×10^5
∅8	305	483	2.1×10^5
∅12	409	578	2.0×10^5
∅18	345	465	2.0×10^5

conforms to the following details: (1) The ratio of the thawing duration to the duration of one cycle must be greater than ¼. (2) The ratio of the time when the temperature changes from 3 to 16 °C to the total time of the freezing process in the chamber must be greater than ½.

2.3. Instrumentation and test procedures

The test setup and measurement configuration are shown in Fig. 4. Linear variable displacement transducers (LVDTs) were installed to monitor lateral and shear displacements. The lateral displacements at the loading point were measured by a horizontal LVDT, which had a height of 800 mm to the upper surface of the foundation block. To record the foundation slip, another LVDT was used at the centerline of the foundation block. Shear deformation were measured by two 45° crossed LVDTs attached to the four corners of the wall specimens. Due to the crushing of the compression toes, the bottom ball joints fixing the two LVDTs set to measure shear deformation typically came off during the testing procedure. To measure the total damage of the specimen, the ball joint was fixed onto the upper surface of the foundation block in the same location as the ball joint of the wall corners.

First, the target vertical load was exerted on the specimens via hydraulic jacks. Then, the actuator attached to the top of the specimen through the lateral load transfer assembly applied a lateral load; the vertical load was held constant throughout the testing process. However, it was difficult to identify the yielding state of the specimens that failed by the brittle failure mode. The equation built by Hirosawa [22] was used to predict the yielding load of wall SW-1 using the real material strengths. The calculation result (270 kN) was used as the yielding load for wall SW-1. When the diagonal cracks near the wall center were first detected, and the loading stiffness began to decrease by observing the machine

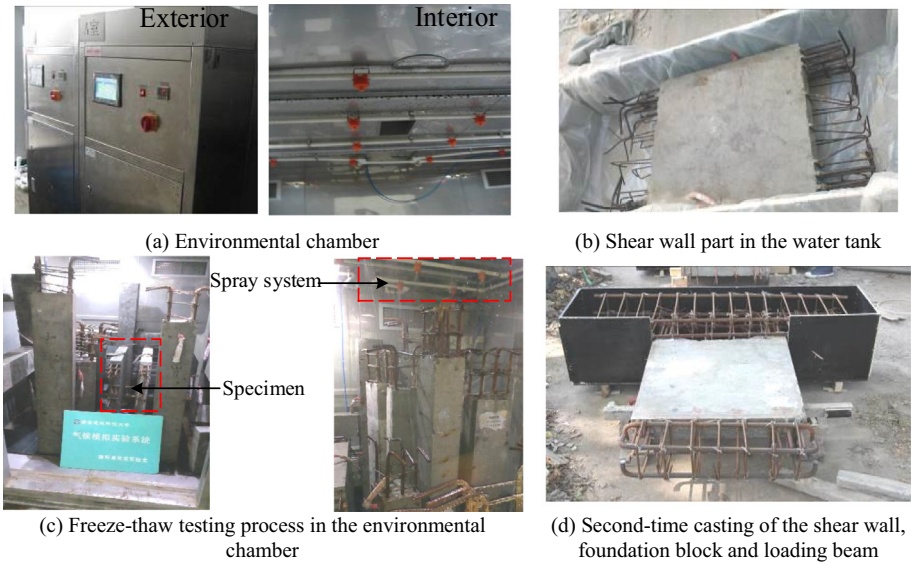

(a) Environmental chamber

(b) Shear wall part in the water tank

(c) Freeze-thaw testing process in the environmental chamber

(d) Second-time casting of the shear wall, foundation block and loading beam

Fig. 2. Photos of the freeze-thaw testing process.

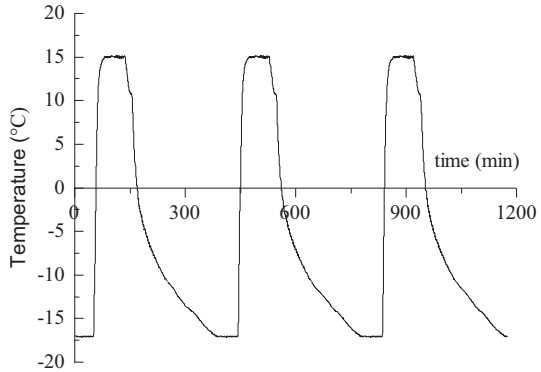

Fig. 3. Environmental parameters in the environmental chamber.

hysteric curves, the specimens were considered to be yielding for wall SW 2 through 4. Prior to the yielding of the specimen, the lateral load was exerted by the force-controlled mode. After the yielding of the specimen, three cycles of loading and unloading were conducted for each subsequent displacement level, which increased by an incremental displacement of 1 mm (drift ratio = 0.125%) [23,24]. Fig. 5 shows the loading history of the wall specimens.

In force-controlled cycles, the load increment was constant as ±30 kN for each step. The real drift level for walls SW-1 through 4 are shown in Table 3.

3. Experimental results and observations

3.1. Residual strength of concrete that experienced FTCs

The method of testing concrete strength with a drilled core was used to measure the residual strength of the concrete specimens. The drilled cores are standard cylinders with diameters and heights of 100 mm, as shown in Fig. 6(a) and (b). Three standard cylinders are used for wall SW-2. Since SW-1, SW-3 and SW-4 were damaged after loading, only two cylinders could be obtained for each wall.

The equivalent compressive strength of a standard test cube of core specimens can be calculated by the following equation [25]:

$$f_{cu}^{e} = \frac{4\beta F}{\pi d^2} \quad (1)$$

where f_{cu}^{e} is the equivalent compressive strength of standard test cube; F is the maximum compressive stress measured by core specimen; d is the average diameter of core specimen; and β is the conversion coefficient of the height-diameter ratio. When height-diameter ratio is equal to 1.0, $\beta = 1.0$.

The residual strength was calculated using Eq. (1), with results shown in Table 4. To reveal the damage mechanisms of squat shear wall specimens under FTCs in the microstructure level, the scanning electron microscope (SEM) test was carried out for specimens after different number of FTCs (SW-1: 0 cycles; SW-2: 100 cycles; SW-3:200 cycles; SW-4: 300 cycles). The SEM test results are given in Fig. 7. As seen from Fig. 7(a) and (b), the internal content of SW-1 specimen appears much denser than SW-2. Floccule appeared in specimen SW-3 (Fig. 7(c)) after 200 cycles and they became interconnected with each other to form as net structure after 300 cycles (Fig. 7(d)). Then, the inside of wall specimens was becoming loose as the number of FTCs increased. As seen from Fig. 6(c), the compressive strength decreased as the number of FTCs increased, which is attributed to the cumulative damage of specimens (including concrete expansion and cracking) induced by successive FTCs, which was consistent with the SEMs of wall specimens.

3.2. Cracking process of wall specimens subjected to frost action

The lengthwise visible cracks along the boundary zone were caused by frost action in wall SW-2, as shown in Fig. 8(a). Most of the cracks were observed in the two side edges of the wall; transverse hairline cracks were also detected. As the number of FTCs increased to 200, the number of cracks present increased, and the transverse cracks began to widen and extend. These cracks were found primarily around the sides of wall SW-3, and several cracks also appeared in the wall center. The baring of certain aggregates along boundary edges was detected, as shown in Fig. 8(b). When the number of FTCs increased to 300, the number of cracks also increased, and the transverse cracks widened and extended to the center of wall SW-4. The concrete along the boundary edges began to loosen, and some aggregates and mortar began to fall off, as shown in Fig. 8(c). Many horizontal cracks were still observed at the top and bottom of the wall; short vertical cracks were also detected at the bottom of the wall; and a horizontal crack was also observed near the wall center after wall SW-4 had been painted white for the test, as shown in Fig. 8(d).

Note that the wall edges were subjected to two-dimensional frost action, and the wall webs were subjected to one-dimensional frost action during the FTCs; thus, the frost cracks propagated from the wall edges to the center of the wall, which agreed with the frost-crack spreading process. Based on the theory of hydrostatic and osmotic pressures, when the inner tensile stress caused by hydrostatic and osmotic pressures exceeded the tensile

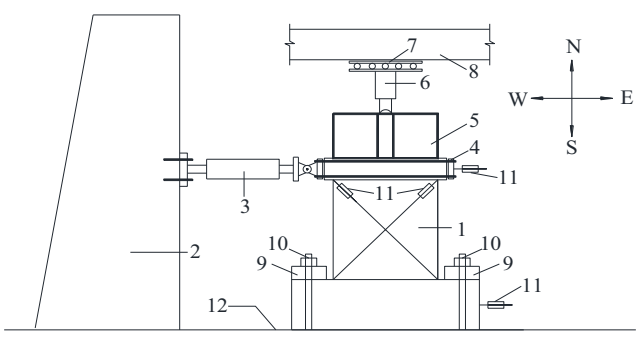

1. Wall Specimen 2. Reaction Wall 3. Hydraulic Actuator 4. Lateral Load Transfer Aassembly
5. Rigidity Beam 6. Hydraulic Jack 7. Sliding Support 8. Reaction Beam
9. Rigidity Anchorage Beam 10. Rolled Screw 11. LVDTs 12. Strong Floor

Fig. 4. Test setup and arrangement of instruments.

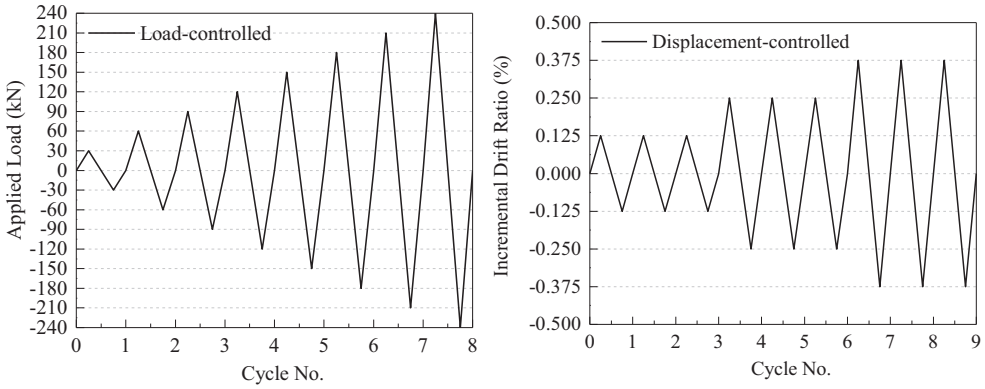

Fig. 5. Loading protocol.

Table 3
Real drift level for SW 1–4.

Specimen number	Load-controlled		Displacement-controlled			Total number of cycles (times)
	First step (kN)	Final step (kN)/drift ratio (%)	Drift ratio (%)/cycle (times)	Drift ratio (%)/cycle (times)	Drift ratio (%)/cycle (times)	
SW-1	30	270/0.41	0.53/3	0.63/3	0.73/2	17
SW-2	30	210/0.23	0.38/3	0.52/3	0.75/3	16
SW-3	30	240/0.40	0.52/3	0.63/3	0.74/2	16
SW-4	30	210/0.46	0.57/3	0.69/3	0.81/2	15

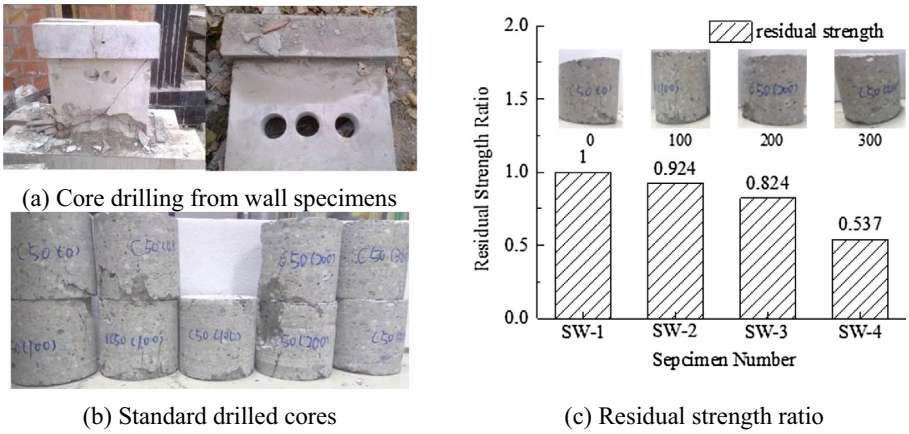

(a) Core drilling from wall specimens

(b) Standard drilled cores

(c) Residual strength ratio

Fig. 6. The residual strength measured by core drilling.

Table 4
Concrete residual strength of different freeze-thaw cycle.

Concrete strength grade	Designed freeze-thaw cycle (no)	f^e_{cu} (MPa)	f_{cu} (MPa)	f^e_{cu}/f_{cu}
C50	0	53.73	55.08	0.975
	100	49.64		0.901
	200	44.25		0.803
	300	28.86		0.524

strength of concrete, internal micro cracks in the concrete began to spread as the number of FTCs increased; the micro cracks then began to extend and interconnect such that the number of cracks increased more rapidly, while the cracks widened [4].

3.3. Damage process and failure pattern

The final damage states and crack maps of the four specimens are shown in Fig. 9. For the control wall SW-1, the first horizontal crack appeared at the bottom of the wall boundary zone when the horizontal load reached 168.89 kN, and the corresponding horizontal displacement was 1.27 mm (*drift ratio* = 1/630). As the load amplitude increased, new horizontal short cracks were detected from the bottom to the top of the specimen along the two sides of the boundary zone. Certain parts of the initial horizontal cracks were found to extend downward to the bottom of the wall along a 45° diagonal line when the cracks reached the web wall, as shown in Fig. 10(a), which indicated that the response of wall SW-1 was initially dominated by flexural cracking.

When the real horizontal displacement reached 3.25 mm (*drift ratio* = 1/250), diagonal cracks appeared on the wall, and the loading stiffness of wall SW-1 decreased markedly. Then, the control mode of the load was switched from the force-controlled mode to the displacement-controlled mode. As the displacement amplitude increased, the inclined shear cracks that form in each direction began to dominate the wall and intersect each other due to cyclic loading; then, a diagonal corner-to-corner crack appeared and widened. Finally, the maximum crack width of the

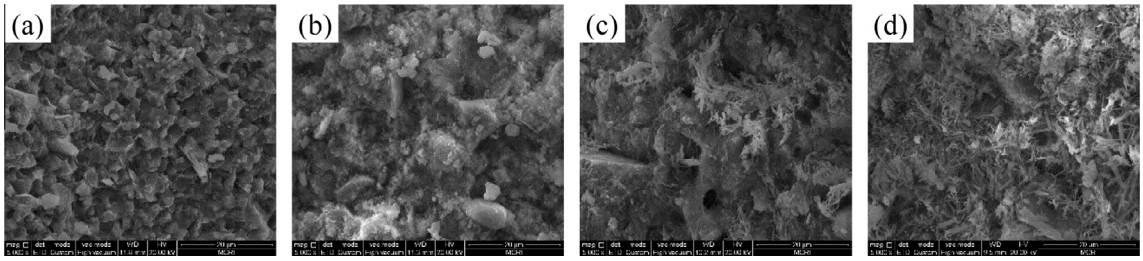

Fig. 7. SEM micro-photographs (magnify 5000 times) of wall specimen after different FTCs: (a) 0 cycles (SW-1); (b) 100 cycles (SW-2). (c) 200 cycles (SW-3). (d) 300 cycles (SW-4).

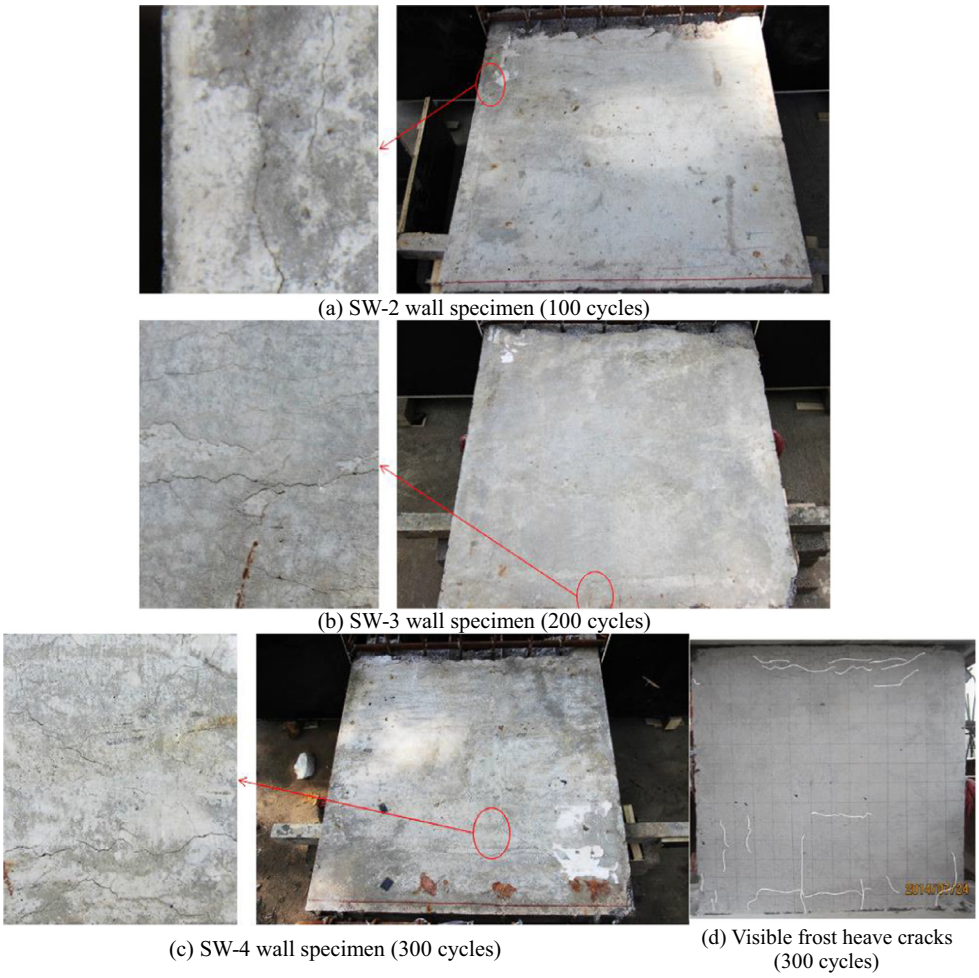

Fig. 8. Cracking process of wall specimens subjected to frost action.

corner-to-corner crack reached 1 mm, and a small portion of the concrete cover located in the center of wall spalled, as shown in Fig. 9(a).

For wall SW-2, the sequences of observed damage were similar to wall SW-1 throughout the loading process. The horizontal cracks initially dominated wall SW-2, and fewer portions of the cracks extended downward to the bottom of the wall as the drift increased. A small number of inclined cracks appeared at the four corners of the wall web, and only four cracks became connected, forming the primary cracks, as shown in Fig. 9(b). Finally, the primary cracks widened and propagated into the compression toe of the wall due to cyclic loading as the displacement amplitude increased.

Note that the failures of walls SW-1 and SW-2 were characterized by one wide inclined cracks with respect to each loading direction. Cracking was not widespread over the wall web; the damage was concentrated in the inclined cracks, and the walls failed by diagonal tension [26].

For wall SW-3, the initial inclined crack was detected at the bottom of the boundary zone in the wall web when the load-controlled level reached 180 kN, as shown in Fig. 10(b). The location and angle of the first cracks in wall SW-3 were different from those in walls SW-1 and SW-2. In the load-controlled mode, where the load was set to 210 kN, two intersecting diagonal cracks dominated the wall, as shown in Fig. 10(c), and then extended to the left edge and bottom of the wall as the load reached 240 kN in the load-controlled mode. As the displacement amplitude increased, another diagonal crack appeared at the bottom of the right boundary zone and then extended to the top of the wall

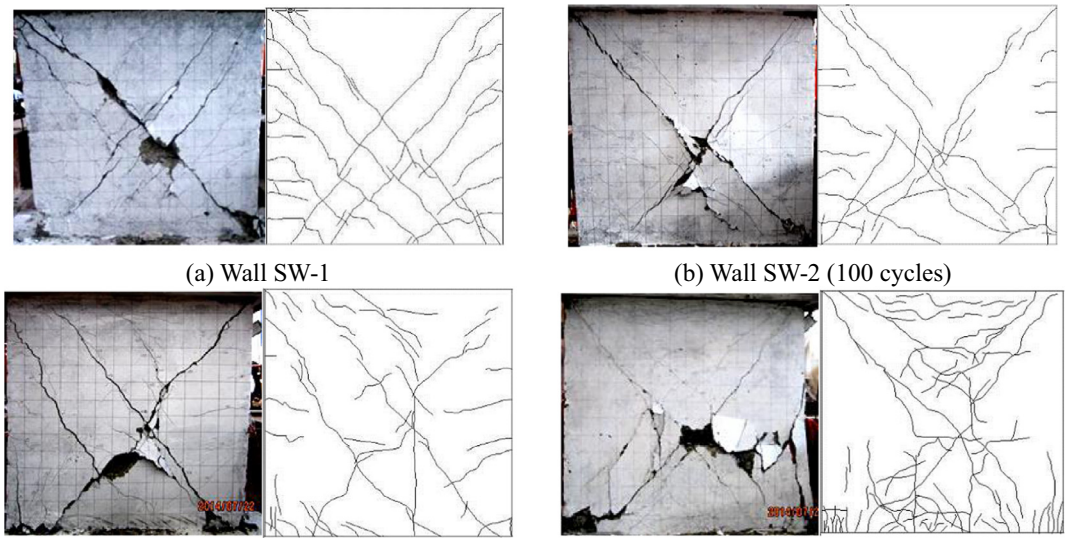

(a) Wall SW-1

(b) Wall SW-2 (100 cycles)

(c) Wall SW-3 specimen (200 cycles)

(d) Wall SW-4 specimen (300 cycles)

Fig. 9. Photographs of wall specimens after testing.

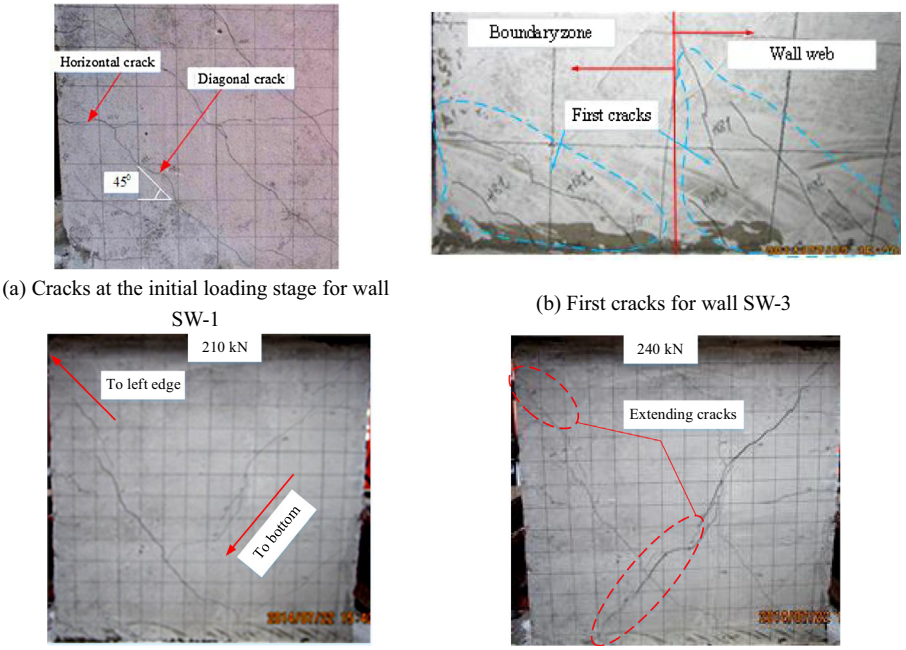

(a) Cracks at the initial loading stage for wall SW-1

(b) First cracks for wall SW-3

(c) Extension of the primary cracks of wall SW-3

Fig. 10. Cracks propagating during the loading process.

web, forming a primary crack. The primary cracks widened due to cyclic loading, and spalling of the concrete cover occurred at the bottom of the boundary zone. The stability of the right compression toe was thus compromised by propagation of the diagonal cracks into this region, and then, the wall failed by diagonal tension, as shown in Fig. 9(c).

For wall SW-4, the inclined crack was first observed at the bottom of the wall web; then, more inclined cracks were detected at the four corners of the wall web. These cracks were generally inclined at approximately 45° and extended to the center of the wall web and connected with each other to form two primary cracks as the lateral displacement increased. After the two primary cracks had formed, cracking was not widespread over the wall web, while the vertical cracks were observed at the bottom of the boundary zones and extended upward to the intersection of the two primary cracks as the drift increased, as shown in Fig. 11(a). Finally, crushing of the concrete struts in the wall web triggered a diagonal compression failure, as shown in Fig. 9(d). The buckling of all boundary longitudinal bars and the crushing of the concrete in the compression toe were detected in the final cycle, as shown in Fig. 11(b). Removing the spalling concrete, a clear boundary was found between the frost and fresh portions of the wall section, as shown in Fig. 11(c) and (d).

In all four walls, the primary diagonal shear cracks were generally inclined at approximately 45° near the wall center. The inclination of the shear cracks significantly decreased towards the web boundaries due to the heavily reinforced boundary elements. Note that the shear crack density was higher for the intact wall SW-1

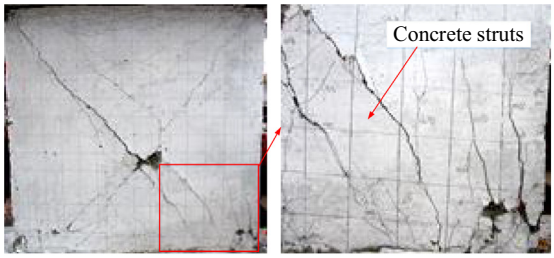

(a) Vertical cracks and concrete struts formed by the inclined cracks for wall SW-4

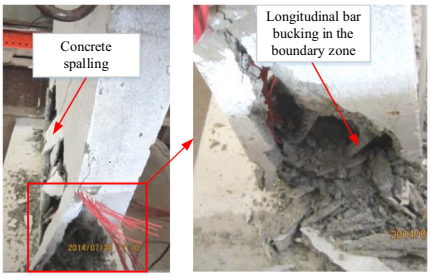

(b) Concrete spalling and boundary longitudinal bar bucking

(c) Concrete layering

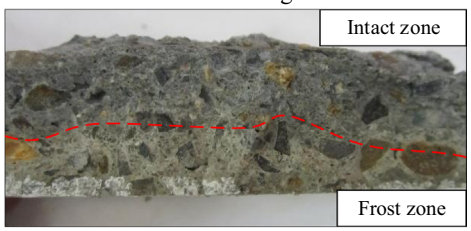

(d) Boundary between the frost and intact portions of the wall

Fig. 11. Damage details for wall SW-4.

and deceased with an increasing number of FTCs. The primary diagonal cracks were observed earlier with an increase in the number of FTCs. The first cracks gradually converted from horizontal to 45° orientations.

4. Experimental interpretation and analysis

4.1. Hysteresis behavior

The hysteretic curves of the lateral load vs. the top displacement for the four specimens are plotted in Fig. 12. Note that all specimens generally show a deterioration in the strength and stiffness of the specimens after the first cycle at a given displacement level. As the number of FTCs increased, the hysteretic loops approached the horizontal axis, and the peak load and initial stiffness of the hysteretic loops decreased significantly at the same displacement level. In this study, residual displacement is defined as the zero-force displacement intercept. The residual displacement increases with the lateral displacement for walls SW 2 through 4, and the hysteretic loops increased significantly at the same displacement level as the number of FTCs increased. Compared to the other three specimens, significant residual displacement and pinched hysteretic behavior were shown clearly in the load-displacement relationships for wall SW-4 in the latter stages of the test. The residual displacement was small and remained constant throughout the loading stage for wall SW-1. The pinched hysteretic behavior was not detected in walls SW 1 through 3.

The effect of the FTCs on the hysteretic behavior of the specimens is significant. Table 5 lists the damage characteristics recorded for all specimens.

4.2. Characteristic parameters of skeleton curves

The equivalent energy method was used to calculate the yielding load of the wall specimens. As shown in Fig. 13, the area of shaded portion A1 was equal to that of shaded portion A2. The ultimate state was defined by the point on the descending section of the envelope curve with a 15% force degradation for the walls that failed via the ductile mode. When the walls failed via the brittle mode, the ultimate state was defined by the damaged point on the envelope curve [19]. Skeleton curves of the wall specimens are plotted in Fig. 15.

Ductility is characterized by the displacement ductility coefficient as [22]:

$$\mu_\Delta = \Delta_u/\Delta_y \tag{2}$$

where Δ_u and Δ_y are the ultimate and yielding displacement, respectively.

Plastic rotation is calculated as [27]:

$$\theta_p = (\Delta_u - \Delta_y)/H \tag{3}$$

where H is the calculated height of the wall. Table 3 lists the damage characteristics recorded and calculated for all specimens.

(1) Influence of FTCs on the load-carrying capacity

Note that the cracking, yielding and peak loads decreased as the number of FTCs increased except for the cracking load of wall SW-2, which might be attributed to the minor variation on the pouring quality of concrete, and at the same time, residual strength of SW-1 and SW-2 has been preserved due to the small number FTCs for SW-2, as indicated in Fig. 6. The yielding load decreased from 276.77 to 188.75 kN (31.80%), and the peak load decreased from 330.35 to 231.30 kN (29.89%) when the number of FTCs increased from 0 to 300; these results indicated that the effect of the FTCs on the load-carrying capacity was considerable.

(2) Influence of FTCs on the deformation capacity

The cracking displacement increased from 1.27 to 1.47 (15.7%), and the yielding displacement decreased from 3.25 to 2.77 mm (14.77%) when the number of FTCs increased from 0 to 300. The yielding displacement of wall SW-3 increased by 6% compared to that of wall SW-2. The peak displacement fluctuated upward between 0.5% and 1.9% as the number of FTCs increased for walls SW 1 through 3 but fluctuated downward by 6% for wall SW-4, which could be attributed to the change from diagonal tension to diagonal tension in the failure mode. These results showed that

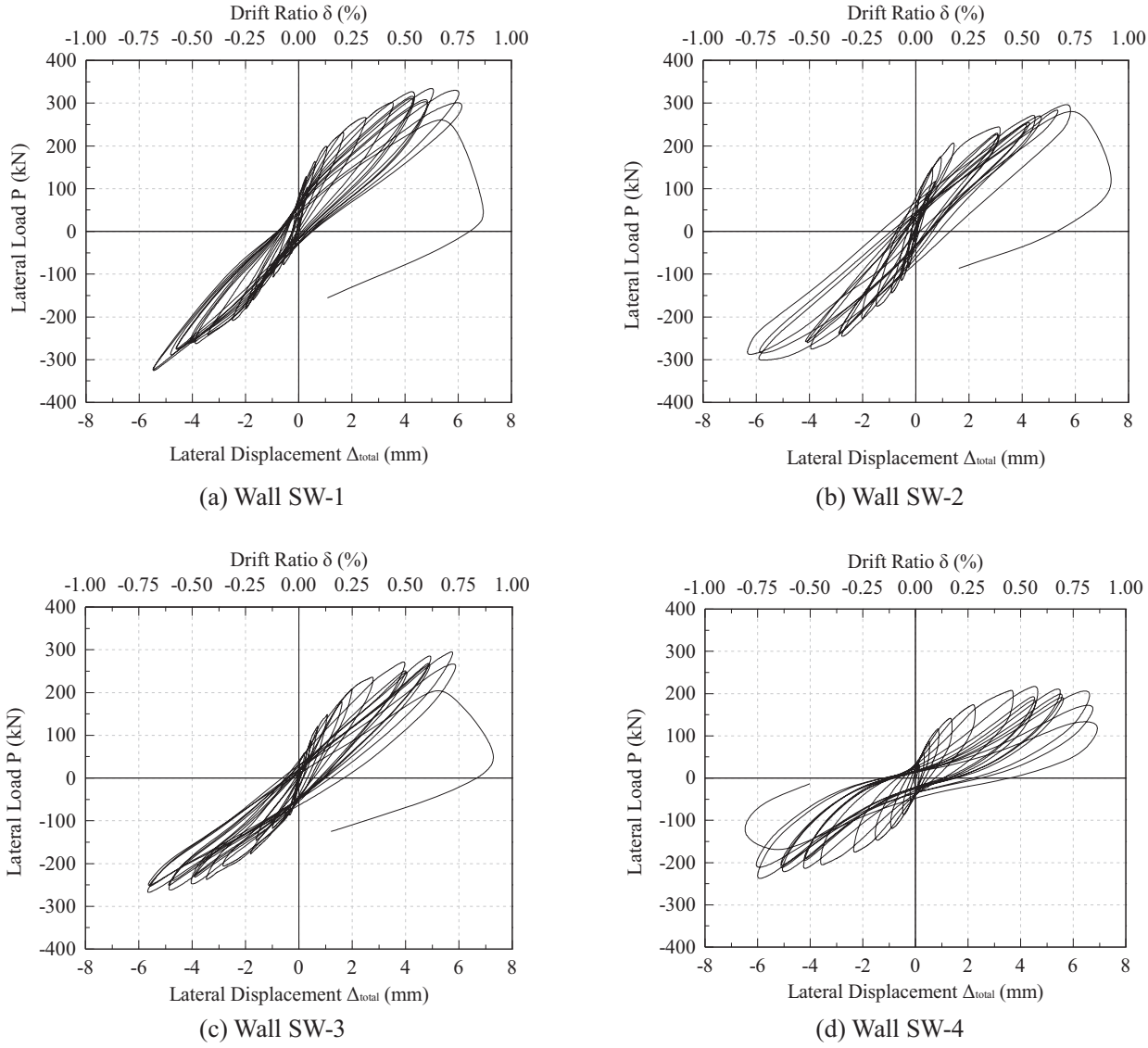

Fig. 12. Hysteric curves of wall specimens.

Table 5
Characteristic parameters of skeleton curves.

Specimen number	Cracking point		Yielding point		Peak point		Ultimate displacement Δ_u/mm	Ductility coefficient μ_Δ	Plastic rotation θ_P (%)
	P_c/kN	Δ_c/mm	P_y/kN	Δ_y/mm	P_p/kN	Δ_p/mm			
SW-1	168.89	1.27	276.77	3.25	330.35	5.86	5.86	1.80	0.326
SW-2	179.41	1.25	248.41	2.97	302.92	5.97	5.97	2.01	0.375
SW-3	151.37	1.38	238.63	3.15	288.50	5.89	5.89	1.87	0.343
SW-4	149.31	1.47	188.75	2.77	231.60	5.51	6.51	2.35	0.468

the effect of the FTCs on the peak displacement was not considerable, as shown in Table 5.

The results indicated that the load-carrying parameters, such as yielding and peak loads, were more sensitive to the FTCs than the displacement parameters and decreased considerably as the number of FTCs increased.

The ductility coefficient of all specimens ranged between 1.80 and 2.35, indicating a brittle failure mode. The ductility coefficient and plastic rotation of all specimens increased overall as the number of FTCs increased. The ductility coefficient and plastic rotation of wall SW-4 increased by 30.56% and 43.56%, respectively, compared to wall SW-1.

(3) Discussion on ductility coefficient

It has been experimentally concluded and verified by several researchers that compressive strength of both unconfined and confined concrete decreased and peak strain increased as the number of FTCs increased [2,11,13,14,16–18], that is to say, concrete become softener and softener. For the confined concrete specimens with concrete cubic strength of 45.2 MPa, Duan [18] found that the descending branches of the stress-strain curve of the frozen-thawed specimens underwent 300 FTCs dropped more slowly than the un-frozen-thawed specimens, meaning that the ductility ratio of the frozen-thawed specimens was higher. This phenomenon

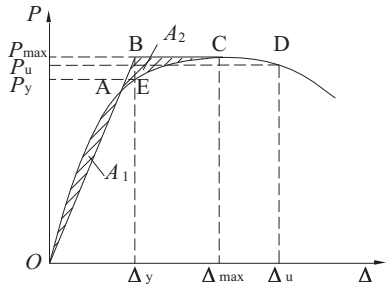

Fig. 13. Definition of yielding displacement.

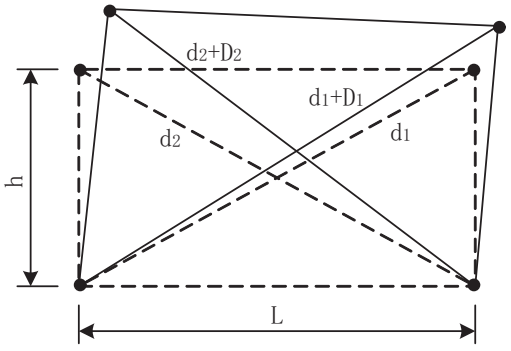

Fig. 14. Simplified method to determine the shear deformation of a wall section.

would be attributed to the fact that the damage at the bonding interface caused by FTCs was not severe. Meanwhile, the concrete strength decreased as the number of FTCs increased, resulting in an increase in the real confinement index λ ($\lambda = \rho \cdot f_{yh}/f_c$, where f_{yh} is yield strength of the transverse ties, f_c is the prismatic strength of plain concrete, and ρ is the volumetric ratio of confining steel) and a higher confinement.

In this experiment, the compressive strength of standard test cube is 55 MPa, which is higher than the concrete cubic strength of 45.2 MPa by Duan [18]. Similarly, it can be reasonably concluded that, for the RC shear wall damaged by FTCs, the ductility ratio of the concrete stress-strain curve in the boundary zone of wall specimens would increase as the increase of FTCs. Therefore, since the increase of the concrete peak strain and confinement index is benificial in improving the ductility of the shear walls, the specimens that experienced more FTCs tend to have larger ductility coefficients and plastic rotations.

To determine more details about the effects of the FTCs on the hysteretic behavior of the specimens, the total displacement was divided into two portions: the shear displacement and the flexural displacement. More detail was introduced as follows.

4.3. Shear deformation analysis

Shear deformations can be calculated directly from the "X" configuration shown in Fig. 14 [28]:

$$\Delta_s = \frac{1}{2}\left[\sqrt{(d_1+D_1)^2-h^2} - \sqrt{(d_2+D_2)^2-h^2}\right] \quad (4)$$

where d_1 and d_2 are the original lengths of the two diagonal sensors; D_1 and D_2 are the displacements measured from these diagonal sensors; and h is the height of the wall.

Based on Eq. (4), the shear rotation of the wall can be calculated as:

$$\gamma = \frac{\Delta_s}{h} \quad (5)$$

The hysteretic curves of lateral load vs. top shear displacement for the four specimens are plotted in Fig. 16. The shear distortion and contribution of shear deformations at the cracking, yielding and peak points are shown in Fig. 17(a) and (b), respectively. Table 6 lists the shear distortion at three key points with the ratio of its contribution to the total displacement for all specimens.

The shear distortion increased from 0.0306% rad to 0.106% rad by 247% at the cracking point, increased from 0.108% rad to 0.216% rad by 99% at the yielding point, and increased from 0.174% rad to 0.463% rad by 166% at the peak point when the FTCs increased from 0 to 300, as shown in Fig. 17(a) and Table 6. The contributions of the shear displacement at the peaking points were 29.7%, 41.8%, 59.4%, and 84.1% for walls SW 1–4, respectively, as shown in Fig. 17(b). The average contributions of the shear deformations at three key points, such as cracking, yielding and peaking point, were approximately 29%, 38%, 48%, and 78% for walls SW 1–4, respectively. The ratio of the shear displacement to the total displacement increased as the number of FTCs increased, as shown in Fig. 17(b).

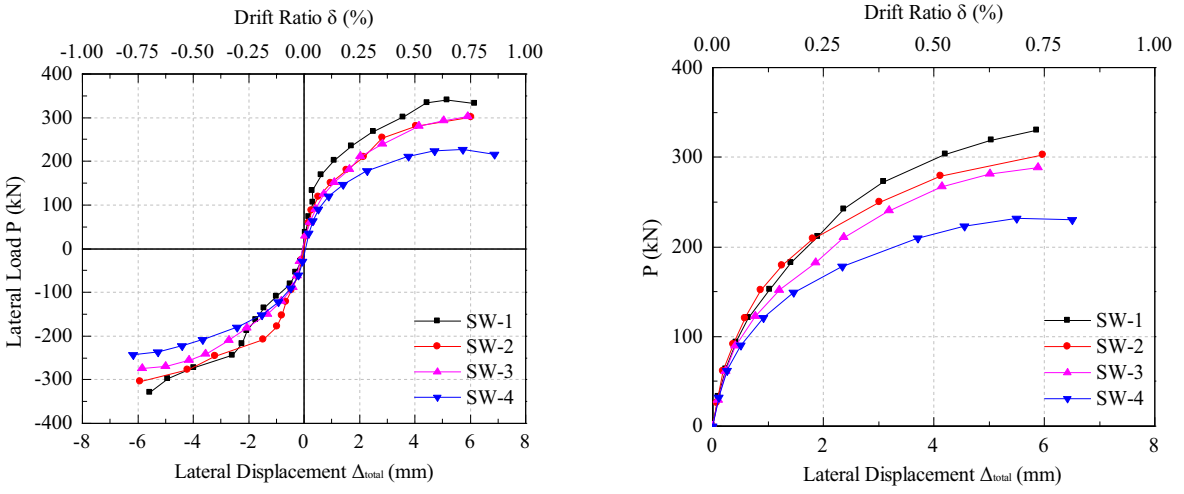

(a) Experimental skeleton curve (b) Average skeleton curve

Fig. 15. Skeleton curves of wall specimens.

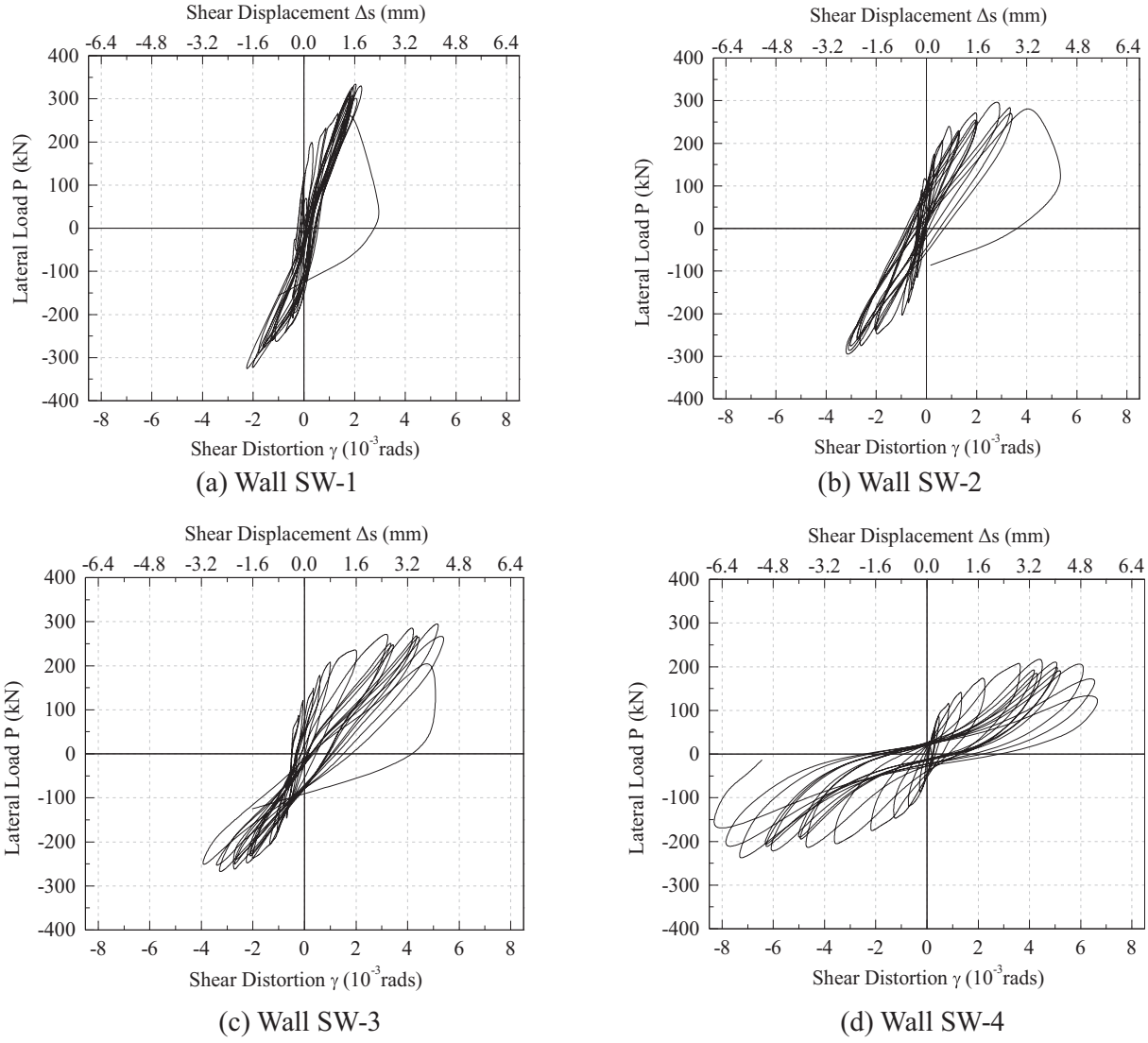

Fig. 16. Hysteric curve of the shear distortion.

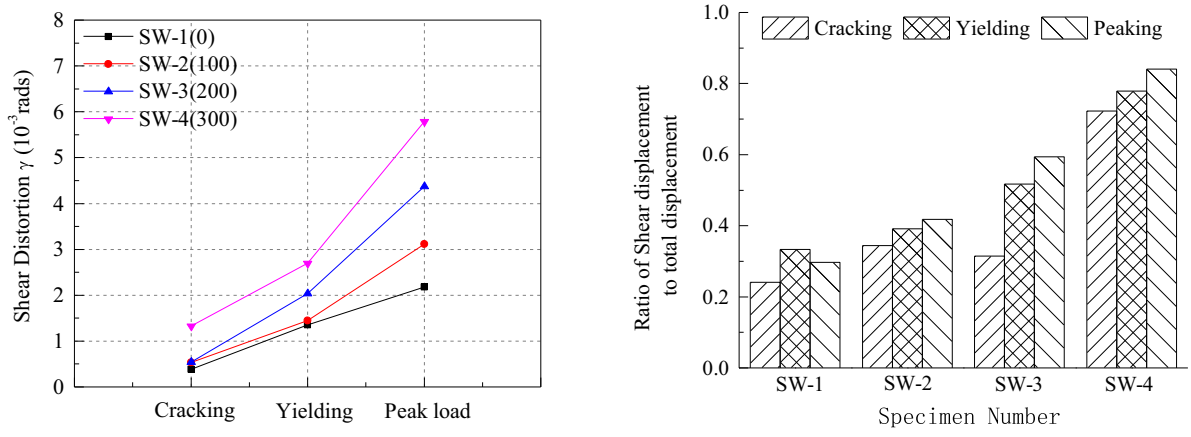

Fig. 17. Shear distortion and contribution of shear deformations at the key points.

Table 6
Shear deformation analysis.

Specimen number	Cracking point		Yielding point		Peaking point	
	$\gamma/10^{-3}$ rad	Δ_s/Δ	$\gamma/10^{-3}$ rad	Δ_s/Δ	$\gamma/10^{-3}$ rad	Δ_s/Δ
SW-1	0.306	0.241	1.082	0.333	1.743	0.297
SW-2	0.430	0.344	1.161	0.391	2.494	0.418
SW-3	0.434	0.314	1.630	0.517	3.498	0.594
SW-4	1.062	0.723	2.156	0.779	4.632	0.841

Notes: Δ_s/Δ represents the ratio of the shear displacement to the total lateral displacement.

4.4. Contribution of the two components to the total lateral displacement

The flexural displacement (Δ_f) at the loading point of the wall are calculated by subtracting the shear displacement (Δ_f) from the total lateral displacement (Δ_{total}) [29]:

$$\Delta_f = \Delta_{total} - \Delta_s \tag{6}$$

The flexural displacements were found to decrease as the number of FTCs increased, as shown in Fig. 18.

The contribution of the shear to the total displacement remained similar from the beginning to the end of the test for wall SW-1, as shown in Fig. 19(a); the average contributions of shear deformations above the 120 kN load level were approximately 29% for wall SW-1. The contribution of the shear displacement component generally increased from the beginning of the test until the end of the test for walls SW-2, SW-3 and SW-4. The average contribution of the shear to the total displacement increased from 29% to 79% (172%) when the number of FTCs increased from 0 to 300. The trend of the flexural displacement contribution to the

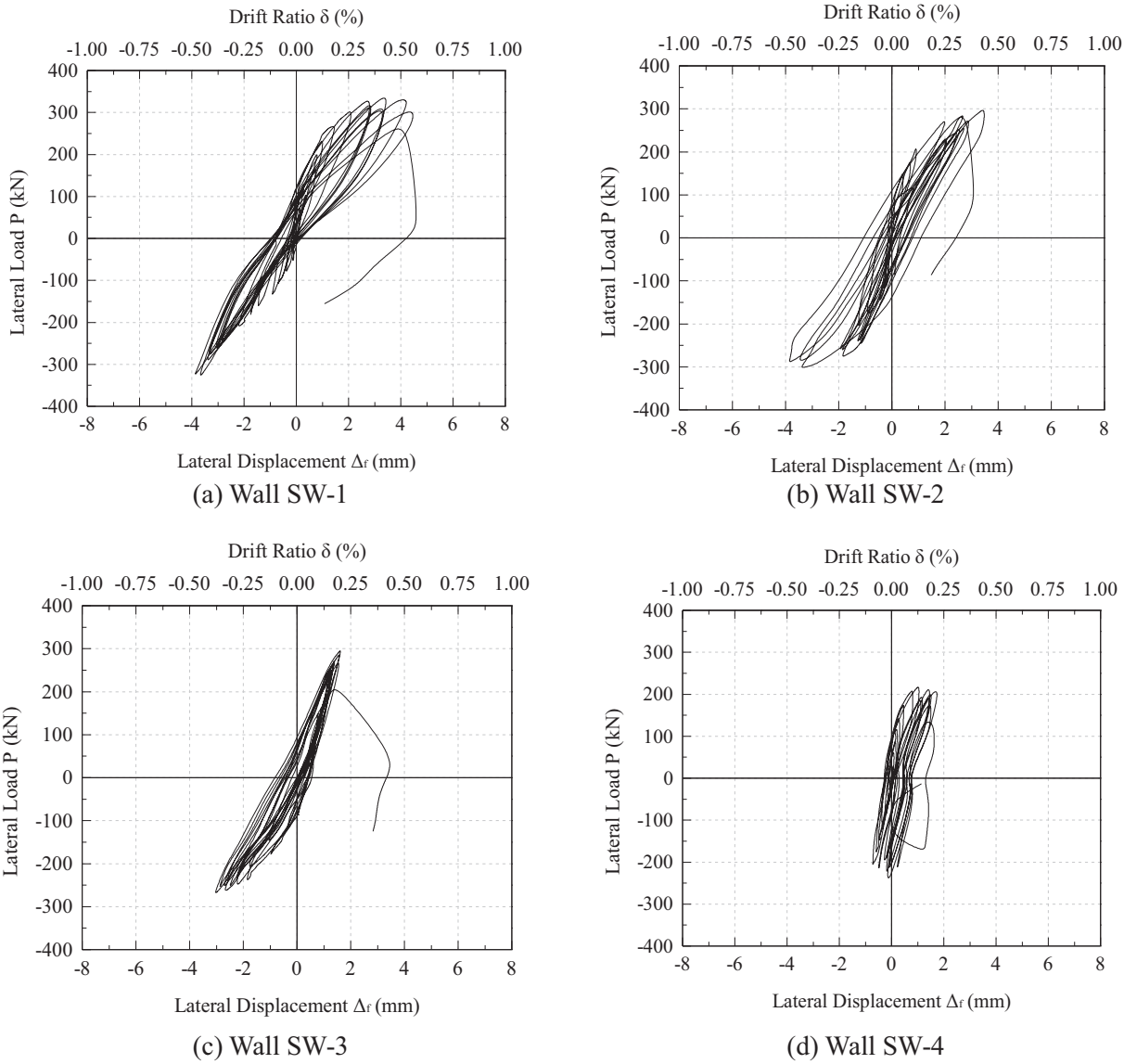

Fig. 18. Hysteric curves of the flexural displacement.

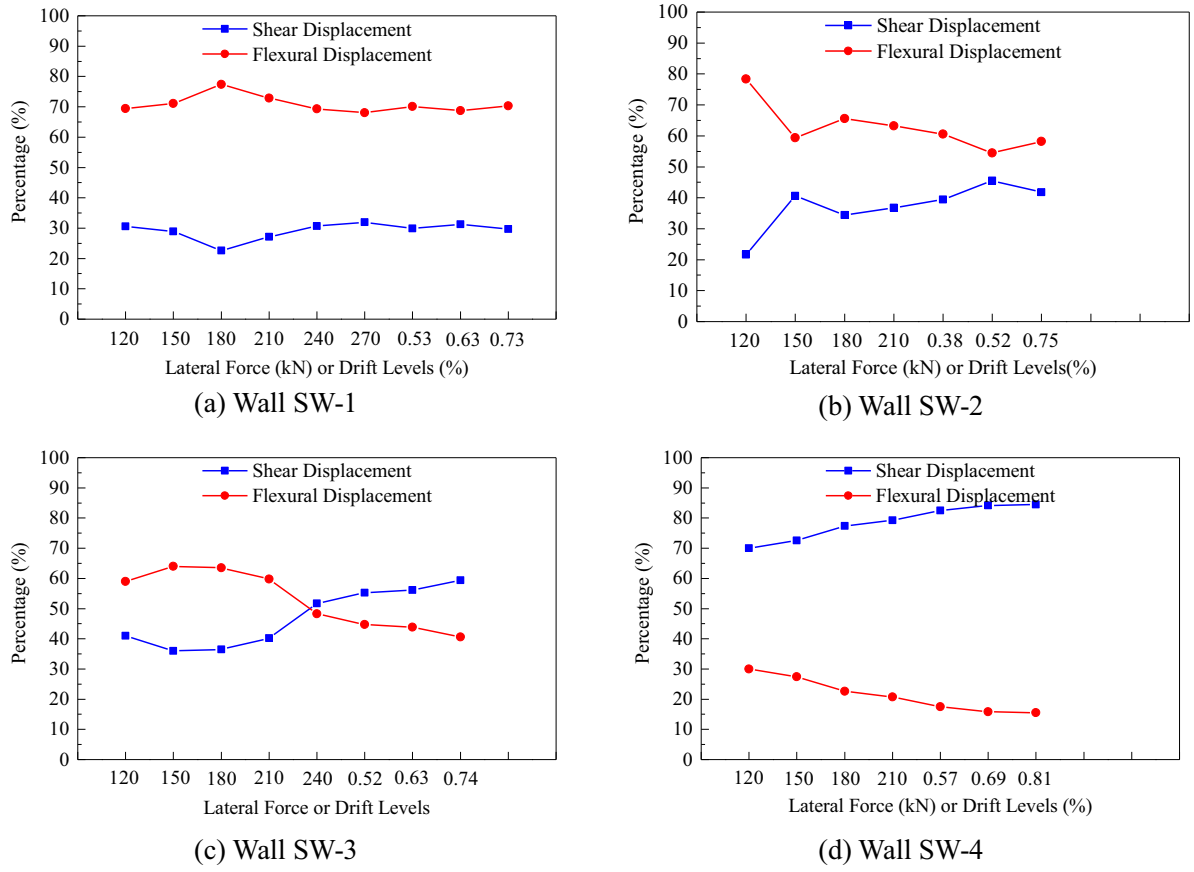

Fig. 19. Contributions to top lateral displacement.

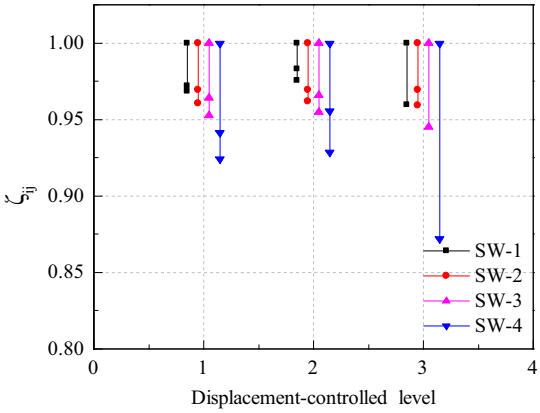

Fig. 20. Strength degradation law of wall specimens.

total displacement opposed the trend of the shear contribution, as shown in Fig. 19.

4.5. Strength degradation

The hysteretic curves of all of the specimens showed that strength decreased as the number of loading cycles with the same controlled displacement increased. This phenomenon is called strength degradation and can be described by the strength degradation coefficient ζ_{ij}, which is defined as the ratio of peak loads of the ith cycle to the first cycle under the same controlled displacements as the j drift ratio level. The relationship between ζ_{ij} and the drift ratio level is shown in Fig. 20, which showed that the strength degradation coefficient decreased under the same controlled displacements for the four specimens, and the strength degradation of the second cycle was larger than that of the third cycle. As the number of FTCs increased, the strength degradation coefficient of the second cycle decreased gradually, thus the strength degradation increased more quickly and was affected significantly by the number of FTCs.

4.6. Stiffness degradation

The stiffness of the specimens can be expressed in terms of the secant stiffness K_i [30], which is defined as:

$$K_i = \frac{|+P_i| + |-P_i|}{|+\Delta_i| + |-\Delta_i|} \tag{7}$$

where P_i is the peak load in the first cycle under ith controlled load or displacement, and Δ_i is the displacement corresponding to P_i.

The variation of the secant stiffness of the specimens as the top displacement increased up to ultimate state displacement is shown in Fig. 21. Initially, the stiffness of the specimens decreased quickly. As the displacement increased, the decrease in the stiffness slowed. The change of the secant stiffness degradation rate on the curves was found near the locations of concrete cracking in all specimens. All specimens exhibited nearly identical stiffness degradation rates as displacements increased, as shown in Fig. 21.

4.7. Energy dissipation behavior

(1) Energy dissipation coefficient

The energy dissipation capacity of the specimens is measured by the areas surrounded by the load-displacement curves, as

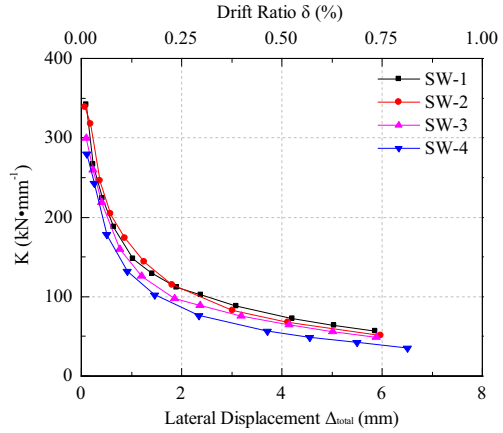

Fig. 21. Secant stiffness coefficient K vs. the top displacement for the four specimens.

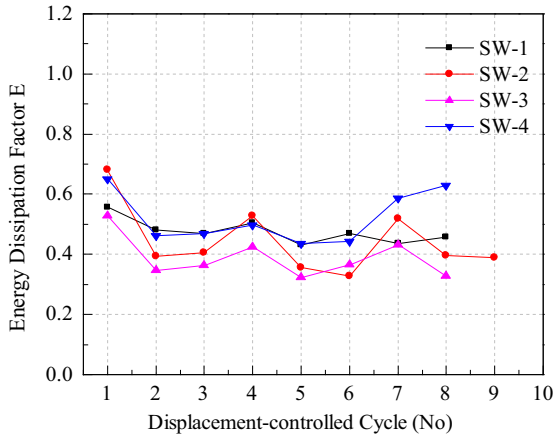

Fig. 23. Curves of the energy dissipation factor vs. the displacement-controlled cycles.

shown in Fig. 22, and is expressed in terms of the energy dissipation coefficient E [30], which is defined as:

$$E = \frac{S_{ABCDA}}{S_{OBE} + S_{ODF}} \tag{8}$$

The increase in the energy dissipation coefficient indicates that the hysteretic hoop is wider; thus, the hysteric behavior becomes more stable, and the deterioration of the strength and stiffness is less significant. The relationship between E and the displacement-controlled cycles for all of the specimens is plotted in Fig. 23. Note that E decreases as the number of cycles increase for walls SW 1 through 3 at the same displacement-controlled level. The average energy dissipation coefficient decreases from 0.4757 to 0.3886 (31.80%), when the number of FTCs increases from 0 to 200. For wall SW-4, the energy dissipation coefficient is similar to that of wall SW-1 during the first six cycles and increases only in the last two cycles, causing the average energy coefficient of wall SW-4 to increase by 10%.

(2) Work index

The work index defined by Gosain et al. [31] can be calculated as:

$$I_w = \sum_{i=1}^{n} (P_i \Delta_i / P_y \Delta_y) \tag{9}$$

where P_i is the peak load in the ith cycle; Δ_i is the displacement corresponding to P_i, and P_y and Δ_y are the yielding load and displacement, respectively.

The increase in the work index indicated that the hinging region absorbs more energy. Compared to wall SW-1, the work index fluctuated from −2.8% to 2.6% as the number of FTCs increased for walls SW 2–3 but increased by 28.4% for wall SW-4.

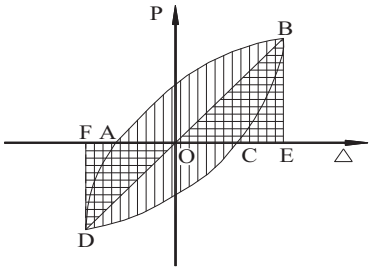

Fig. 22. Calculation diagram of energy dissipation coefficient.

(3) Cumulative hysteretic dissipation energy

The cumulative hysteretic dissipation energy of the specimens increased monotonically as the top displacements increased. For the specimens with different numbers of FTCs, the cumulative dissipation hysteretic energy curves coincide initially and then separate when the top displacements reach 2 mm. The cumulative hysteretic dissipation energy changes irregularly from 2 to 4 mm. The specimens with more FTCs have smaller cumulative hysteretic dissipation energies at the same displacement level when the displacement ranges from 4 to 6 mm. In addition, the cumulative hysteretic dissipation energy of wall SW-4 increases by 25% when the number of FTCs increases from 200 to 300, as shown in Fig. 24.

Table 7 lists the average energy dissipation coefficients, work indexes and cumulative hysteric dissipation energies for all of the specimens. Note that the energy dissipation coefficients and the cumulative hysteric dissipation energies are more sensitive to changes in the number of FTCs than the work index; these parameters also decrease significantly as the number of FTCs increases for walls SW-1 to 3. The energy dissipation coefficient and work index increase by 10% and 28.4%, respectively for wall SW-4.

In the above analyses, the ultimate displacement and energy dissipation capacity indicators show irregular increases when the number of FTCs increased to 300; this result could be attributed to the change in the failure mode and the different reduction ratios in the tensile and compressive strengths caused by the increase in the FTCs. Several studies, including Hassanzadeh and Fagerlund [32], Fagerlund [33] and, Zandi Hanjari et al. [15], have shown that

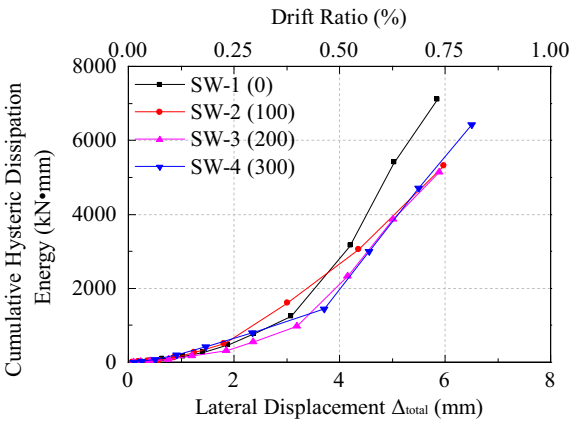

Fig. 24. Curves of the cumulative hysteric energy vs. the lateral displacement.

Table 7
Hysteretic energy dissipation indicators of wall specimens.

Specimen number	E_{dis}	I_w	Cumulative hysteric dissipation energy (kN·mm)
SW-1	0.4757	16.50	7100.3
SW-2	0.4438	16.03	5307.5
SW-3	0.3886	16.93	5134.2
SW-4	0.5219	21.18	6420.9

Notes: E_{dis} is the average energy dissipation coefficient during the displacement-controlled stage, and I_w is the work index.

the reduction in the tensile strength damaged by the number of FTCs is marginally larger than that in the compressive strength. Based on Section 3.3, the residual concrete compression strength controlled the reversed cyclic behavior of wall SW-4 failed by diagonal compression, while the residual concrete tension strength controlled the reversed cyclic behavior of wall SW-1–3 failed by diagonal tension.

5. Conclusions

Four squat RC shear wall specimens with different FTCs were tested under lateral cyclic loads. The effects of the number of FTCs on the damage characteristics, hysteretic behavior, ductility, secant stiffness degradation and energy dissipation capacity of the specimens were analyzed. The following conclusions can be drawn from the test results:

(1) The regular appearance of initial cracks indicated that the responses of the wall specimens were initially dominated by flexural cracking and then gradually transformed into shear cracking when the concrete strength of the wall webs decreased as the number of FTCs increased.
(2) The damage patterns of the wall specimens changed from diagonal tensile failure to compressive failure as the number of FTCs increased based on observations of the damage processes.
(3) As the number of FTCs increased, the lateral load-carrying capacity and secant stiffness of the specimens decreased significantly; the contribution of shear deformation to total lateral displacement increased gradually, which agrees with the regular appearance and extension of the loading cracks; and the hysteretic behavior became more unstable.
(4) The energy dissipation coefficient and cumulative hysteric energy are more sensitive to changes in the number of FTCs than the work index.
(5) The specimens that experienced more FTCs tended to have larger ductility coefficients and plastic rotations due to the increased concrete peak strain and confinement index.

Due to the complex action of FTCs, more wall specimens should be tested to verify the effects of FTCs on the ductility and energy dissipation capacity of RC walls.

Acknowledgments

This study was supported by the National Key Technology R&D Program under Grant No. 2013BAJ08B03, the Research Fund for the Doctoral Program of Higher Education of China (No. 20136120110003), the Research Fund of Shaanxi Province in China (Nos. 2012K12-03-01, 2011KTCQ03-05, 2013JC16), and the Post-doctoral Research Fund from Xi'an University of Architecture and Technology under Grant No. 6040300603. The authors thank the anonymous reviewers for their constructive comments and advices that helped in improving the quality of this manuscript greatly.

References

[1] Mehta PK. Concrete durability-fifty year's progress. In: Proceedings of 2nd international conference on concrete durability. p. 1–31.
[2] Hasan M, Okuyama H, Sato Y, et al. Stress-strain model of concrete damaged by freezing and thawing cycles. J Adv Concr Technol 2004;2(1):89–99.
[3] Rønning Terje Finnerup. Freeze-thaw resistance of concrete effect of: curing conditions, moisture exchange and materials PhD dissertation. Trondheim: Norwegian Institute of Technology; 2001.
[4] Yazdani Frank. Damage assessment, characterization, and modeling for enhanced design of concrete bridge decks in cold regions PhD dissertation. Department of Civil and Environmental Engineering, North Dakota State University; 2015.
[5] Green Mark, Dent Aaron JS, Bisby Luke A. Effect of freeze-thaw cycling on the behavior of reinforced concrete beams strengthened in flexure with fiber reinforced polymer sheets. Can J Civ Eng 2011;30(6):1081–8.
[6] Powers TC. A working hypothesis for further studies of frost resistance of concrete. Proc ACI J 1945;16(4):245–72.
[7] Powers TC. In: Scholer CF et al., editors. Durability of concrete. Detroit: American Concrete Institute; 1975. p. 1–11.
[8] American Society for Testing and Materials. C666-92. Standard test method for resistance of concrete to rapid freezing and thawing; 1995.
[9] RILEM TC176-IDC2002. Recommendations of RILEM TC 176: test methods of frost resistance of concrete. Paris: RILEMRep; 2001. p. 213.
[10] National Standard of the People's Republic of China. The test method of long-term and durability on ordinary concrete Tech Rep GB/T50082-2009. Beijing (China): National Standard of the People's Republic of China; 2009.
[11] Hasan M. Modeling of stress-strain relationships for concrete damaged by freezing and thawing cycles PhD dissertation. Sapporo: Hokkaido University; 2003.
[12] Shin TS, Lee GC, Chang KC. Effect of freezing cycles on bond strength of concrete. J Struct Eng, ASCE 1988;114(3):637–45.
[13] Marzouk H, Jiang Ka-jiu. Effects of freezing and thawing on the tension properties of high-strength concrete. ACI Mater J 1995;91(6):577–86.
[14] Sun W, Zhang YM, Yan HD, et al. Damage and damage resistant of high strength concrete under the action of load and freeze-thaw. Cem Concr Res 1999;29(9):1519–23.
[15] Hanjari K Zandi, Utgenannt P, Lundgren K. Experimental study of the material and bond properties of frost-damaged concrete. Cem Concr Res 2011;41:244–54.
[16] Duan An, Qian Jiaru. Stress-strain relationship of concrete after freezing-thawing cycles. In: Proceedings of the international conference on durability of concrete structures. Hangzhou: Zhejiang University Press; 2008. p. 329–36.
[17] Duan An, Qian Jiaru. Stress-strain relationship of stirrup-confined concrete subjected to freeze-thaw cycles. Chin J Rock Mech Eng 2010;29(1):3016–22.
[18] Duan A, Jin W, Qian J. Effect of freeze-thaw cycles on the stress-strain curves of unconfined and confined concrete. Mater Struct 2011;44(7):1309–24.
[19] Petersen L, Lohaus L, Polak MA. Influence of freezing-and-thawing damage on behavior of reinforced concrete elements. ACI Mater J 2007;104(4):369–78.
[20] Bishnoi Shashank. Strain variations in concrete subjected to cyclic freezing and thawing Master dissertation. Tokyo: University of Tokyo; 2003.
[21] Wuhuancq. http://www.wuhuancq.com/.
[22] Hirosawa M. Past experimental results on reinforced concrete shear walls and analysis on them. Tokyo (Japan): Building Research Institute, Ministry of Construction; 1975.
[23] National Standard of the People's Republic of China. Code for seismic design of buildings, GB 50011-2010. Beijing: Chinese Architectural Industry Press; 2010.
[24] Ying Zhou, Xilin Lu. Shear wall database from Tongji University; 2010. https://nees.org/resources/869.
[25] China Association for Engineering Construction Standardization. Technical specification for testing concrete strength with drilled core, CECS 03:2007. Beijing: China Planning Press; 2007.
[26] C.K. Gulec, A.S. Whittaker. Performance-based assessment and design of squat reinforced concrete shear walls. MCEER-09-0010; 2009.
[27] FEMA-267b. Interim guidelines. Advisory no. 2, supplement to FEMA 267. Washington, DC (USA): Federal Emergency Management Agency; 1999.
[28] Massone LM, Wallace JW. Load-deformation responses of slender reinforced concrete walls. ACI Struct J 2004;101(1):103–13.
[29] Kolozvari, Kristijan. Analytical modeling of cyclic shear-flexure interaction in reinforced concrete structural walls PhD dissertation. Los Angeles: UCLA; 2013.
[30] Industry Standard of the People's Republic of China. Specification of testing methods for earthquake resistant building, JGJ101-96. Beijing: China Architecture Industry Press; 1997.
[31] Gosain NK, Brown RH, Jirsa JO. Shear requirements for load reversals on RC members. J Struct Eng, ASCE 1977;103(7):1461–76.
[32] Hassanzadeh M, Fagerlund G. Residual strength of the frost-damaged reinforced concrete beams. In: III European conference on computational mechanics solids, structures and coupled problems in engineering, 5–8 June, Lisbon, Portugal.
[33] Fagerlund G. A service life model for internal frost damage in concrete, division of building materials. Lund (Sweden): Lund Institute of Technology; 2004.